
GIVING LIGHT A NEW TWIST WITH STANDARD OPTICAL FIBRES: RAINBOW SPIRAL EMISSION

A PREPRINT

F. Mangini^{1*}, M. Ferraro^{2*}, M. Zitelli^{2*}, V. Kalashnikov², A. Niang¹,
T. Mansuryan³, F. Frezza², A. Tonello³, V. Couderc³, A.B. Aceves⁴, S. Wabnitz^{2,5}

October 31, 2021

¹ Department of Information Engineering (DII), University of Brescia, Via Branze 38, 25123 Brescia, Italy.

² Department of Information Engineering, Electronics and Telecommunications (DIET), Sapienza University of Rome, Via Eudossiana 18, 00184 Rome, Italy.

³ Université de Limoges, XLIM, UMR CNRS 7252, 123 Avenue A. Thomas, 87060 Limoges, France

⁴ Department of Mathematics, Southern Methodist University

⁵ Novosibirsk State University, Pirogova 1, Novosibirsk 630090, Russia

* These authors have contributed equally

ABSTRACT

We demonstrate a new practical approach for generating multicolour orbital angular momentum (OAM) beams. It involves a standard silica optical fibre, with appropriate control of input coupling conditions. Specifically, a properly tilted input laser beam must be injected into the fibre cladding. This spontaneously breaks the fibre axial symmetry by imposing wavefront rotation. In this way, OAM beams can be easily generated even with low-power, continuous-wave (CW) laser sources (e.g., a laser pointer). With a high-power near-infrared femtosecond laser, a visible OAM supercontinuum is generated, that is characterized by a coloured spiral emission in the far field. With control of input coupling conditions, one observes that colours of the spiral spatially self-organize in a rainbow distribution. Our method is independent of the laser source wavelength and polarization. Therefore, standard optical fibres may be used for generating OAM beams in many applications, ranging from communications to optical tweezers and quantum optics.

1 Introduction

Orbital Angular Momentum (OAM) modes are peculiar solutions of Maxwell's equations, characterized by phase singularity, helical wavefront, and propagation direction varying with azimuthal angle [1, 2, 3]. OAM modes are also referred to as spiral beams, for their spiral shape in the far-field. Their main characteristic is the so-called topological charge (TC), an integer number that counts the number of wavefront rotations over one wavelength of propagation. Studies of OAM or spiral beams date back to more than thirty years ago, since their introduction by Allen et al. in 1992 [4]. Over time, interest in OAM beams has increased tremendously, thanks to their widespread potential for applications. These range from telecommunications [5, 6] to quantum optics [7], holography [8, 9], and optical tweezers [10, 11], a research recognized by the award of the 2018 Nobel prize to Arthur Ashkin. Because of their intrinsic nature, spiral beams exhibit a peculiar phase profile that must be superimposed on a laser beam, for introducing the axial symmetry-breaking which is necessary to generate OAM. So far, this has been mostly obtained by means of external optical components [12] which, owing to their volume and polarization dependence, hampers the miniaturization of OAM generators, and limits their use in integrated optics [13]. To overcome these drawbacks, micro- and nano-structured OAM generators were recently introduced [12]. Progress was also made in generating OAM beams with optical fibre systems [14]: e.g., fibre gratings [15, 14], vortex fibres [16, 17], microstructured fibres [18], and mode-selective photonic lanterns [19]. All of these OAM generation techniques require either challenging fabrication processes, or using specialty fibres.

In this work, we propose an entirely different and breakthrough approach for the generation of structured light, such as OAM beams: it only involves the use of standard, telecom silica optical fibres. It consists of focusing a laser beam with proper angles ϑ and φ , inside the cladding at the input facet of the fibre, as sketched in Fig. 1a. This produces an azimuthal component to the beam wave vector, so that when propagating inside the fibre, the beam starts spiralling in the cladding, spontaneously leading to OAM or spiral emission with $TC = \pm 1$ at the fibre output, as shown in Fig. 1b. As a cylindrical waveguide, an optical fibre is a natural beam shaper for OAM beams. Multimode fibres (MMFs) support OAM modes on their own, and are therefore among the most suitable candidates for OAM beam generation. Our method does not require a MMF core, i.e., even a singlemode fibre (SMF) can be used, as long as the fibre cladding is multimode. By our approach, we can easily change the TC sign, and consequently the chirality of the spiral, by just inverting the sign of the incidence angle ϑ . In the nonlinear propagation regime, supercontinuum (SC) generation allows for broadband and high-brightness spectral emission, covering all visible spectrum. We reveal that in the far-field, the SC is a spiral beam, containing a mixture of different colours. Under proper input coupling conditions, these colours spontaneously separate in space, giving rise to spiral-shaped rainbow emission, analogous to conical emission in filamentation, which accompanies high-power laser beam propagation in air [20, 21].

2 Results

Our approach to generate OAM and spiral emission by means of commercial, standard telecom fibres is remarkably simple. We demonstrate that a laser beam, coupled with proper input zenith angle ϑ and azimuth angle φ (see Fig. 1a) into fibre cladding modes carrying OAM, produces a spiral emission in the far-field, independently of its wavelength or polarization. The main conditions on the incidence beam angles are: small zenith angles (e.g., $\vartheta < 2^\circ$), and azimuthal angles such that the projection of the laser beam wave vector on the transverse plane of the fibre (k_t) is tangent to the core/cladding interface, so that its radial component is vanishing (see Fig. 1a). In our experiments, we removed the external plastic coating of the fibre, so that the beam undergoes multiple reflections at the cladding-air interface while moving in its helical path. By exploiting the phenomenon of upconversion luminescence (due to the presence of doping, and of intrinsic and extrinsic defects in MMFs [22, 23]), we could also monitor beam propagation inside the fibre by naked eye (see Methods). In Fig. 1c-e, we report microscope images taken from the top of the MMFs, with proper incidence angles. Here, we can clearly recognize a helical visible emission, associated with an OAM beam twisting around the core-cladding interface. The experimental set-up to study spiral emission is shown in Fig. 1f. As a source for SC generation, we used intense femtosecond laser pulses at the 1030 nm wavelength. As discussed in the Supplementary, we observed that spiral emission can be obtained with shorter wavelengths as well. As it exits the fibre, the beam is collected by an imaging lens to measure the near-field spatial profile and spectrum with a CCD camera and a spectrometer, respectively. By means of a flipping mirror we could also image the far-field. The true-colour picture on the right of Fig. 1b was obtained by matching three different conditions: OAM mode propagation, SC generation, and colour spatial separation. In the following, we investigate these elements one at a time. OAM generation is due to

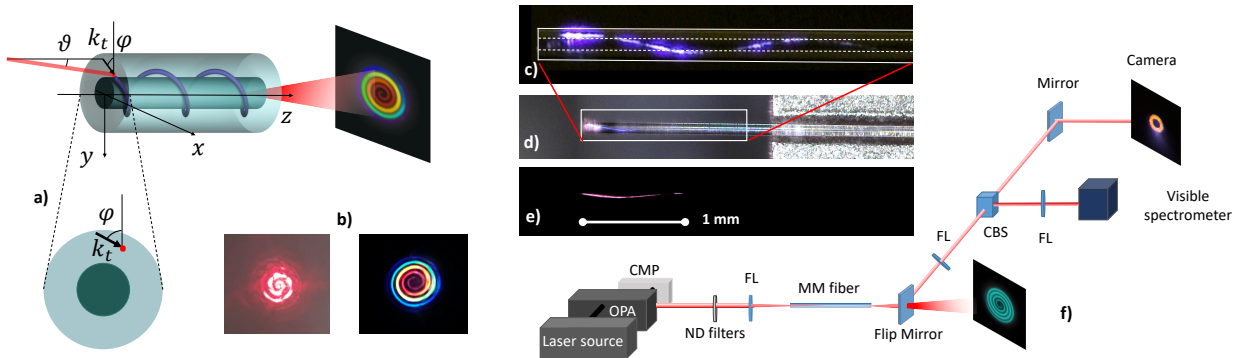


Figure 1: (a) Schematic of fibre geometry and rainbow spiral emission; ϑ is the incidence tilt of the skew ray (or zenith angle), φ is the azimuth angle, and k_t is the projection of the laser beam wave vector on the fibre transverse plane. (b) Spiral emission from CW He-Ne laser (left) or from femtosecond pulse laser (right). (c) Zoom-in of (d), dashed lines indicate core-cladding boundaries. (d) Visualization of helical beam propagation in a graded-index (GRIN) fibre, thanks to upconversion luminescence from material defects and doping. Scattered white light on the right is due to the fibre holder. (e) Same as (d) but from step-index fibre. (f) Schematic of set-up where typical near- and far-fields are shown. The ND filter is used to vary input power, FL stands for focus lens, and CBS for cubic beam splitter.

the excitation of cladding modes supporting OAM both in MMFs and SMFs (see Supplementary). These are excited

when the laser is focused in the cladding with a small tilt angle ϑ (between 1 and 2 degrees), and lead to helical beam propagation as shown in Fig.1c-e. OAM beams are leaky cladding modes, hence they only survive over a short length of fibre (here typically 2 cm), because of core-cladding mode coupling [24]. Light tends to penetrate into the fibre core where the refractive index is higher, and it gets coupled to core modes, while losing its OAM. By limiting the fibre length to a few centimeters, we keep the output transmission above 90% even at MW input powers [25]. Therefore our method permits for a very high OAM conversion efficiency.

Remarkably, our OAM beam generation method is linear, hence it does not require particularly high laser powers. As detailed in the Supplementary, OAM beams could be generated independently of the laser average power and pulse duration. For example, we could generate a red spiral beam by using a CW He-Ne laser (see Fig.1b-left), and even by using a standard laser pointer as a source! OAM generation does not appear to be affected by varying the input state of polarization, and it is wavelength-independent.

Numerical simulations have been performed, in order to reproduce the spiral emission formation. In Fig.2a, we report how a beam that is initially focused on a point, progressively occupies all of the cladding area (see Methods for details of the numerical model). In Fig.2a we also plot the far-field, corresponding to the spatial distribution of the field inside the fibre.

We underline that, in spite of its annular shape in the near-field, the output beam is not an optical vortex, since it does not have the required spiral shape in the phase profile of the corresponding far-field (see the Supplementary Material). To the contrary, the output beam exhibits an intensity spiral shape in the far-field [12]. One can also appreciate that spiral formation requires a certain propagation length (estimated to a few millimeters with our parameters). On the other hand, due to mode coupling with the fibre core, the spiralling far-field vanishes if the fibre is longer than a few centimeters (not shown in the figure). In any case, a strong correlation was observed between the longitudinal domain of spiral existence and the angle of incidence ϑ . Specifically, we noted that as ϑ increases, the range of OAM existence tends to decrease. We estimated both numerically and experimentally the optimal threshold length to be of about 2 cm for $\vartheta \simeq 2^\circ$.

Simulations also explain how to tune the TC of the output beam. Depending on the beam input position, one can reverse the OAM beam chirality, from clockwise to counterclockwise, thus inverting the TC sign. This is illustrated in Fig.2b. Diametrically opposed input positions correspond to opposite winding, hence flipping the TC sign. Excellent qualitative agreement between simulations and experiments was achieved, as shown in Fig.2c-d.

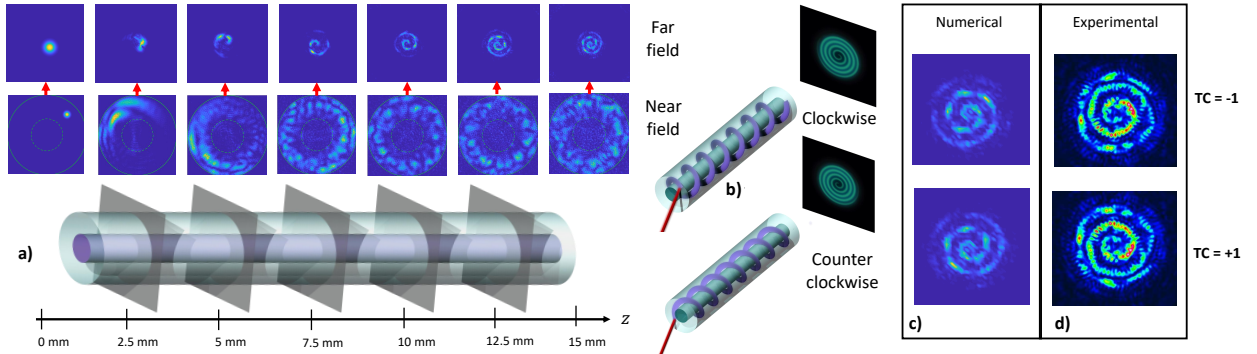


Figure 2: (a) Sketch of the first 1.5 cm of the fibre (bottom); The near-field is numerically computed each 2.5 mm, corresponding to the position where the transverse planes cut the fibre (centre). The far-field is calculated as the Fourier transform of the near-field, showing spiral emission formation (top). (b) Tunability of optical chirality. The spiral emission TC sign depends on the input beam position with respect to the fibre centre. (c) Numerical confirmation of optical chirality inversion. (d) Experimental results corresponding to (c). All simulations and experiments were performed with an input peak power of 3 MW, a wavelength of 1030 nm, $\vartheta = 1.5^\circ$ and $\varphi = 45^\circ$.

Whenever the injected power of a near-infrared femtosecond laser source was high enough to produce SC generation, i.e., a wide nonlinear spectral broadening of the input laser source, a coloured spiral beam exited from the fibre output facet. In Fig.3a,b we report spectra obtained from step-index (SI) and GRIN MMFs, respectively, when varying the input peak power. When the latter reaches 48 MW, the whole visible spectral range is covered, producing all of the images shown in Fig.3c. Due to the absence of clear peaks in the visible range, and because of the nearly symmetric broadening of the pump spectra, we may ascribe the observed SC mechanism to self-phase modulation.

Finally, we could observe that colour spatial separation within the spiral only depends on the input coupling condition, i.e., the position of the incident laser beam on the fibre, while keeping the same spectral composition. In Fig.3c we show that speckled features appear when the input beam is partially focused inside the core. By gradually moving deeper into the cladding, spiral emission becomes clearer, and it is characterized by a disordered mix of colours. Finally, when the beam crosses the cladding-air interface, we obtain the rainbow spiral emission as shown in Fig.1b-right. In our experiments, topological charges other than $TC = 1$ were also observed. An overview of these hybrid order spiral beams is presented in Fig.4.

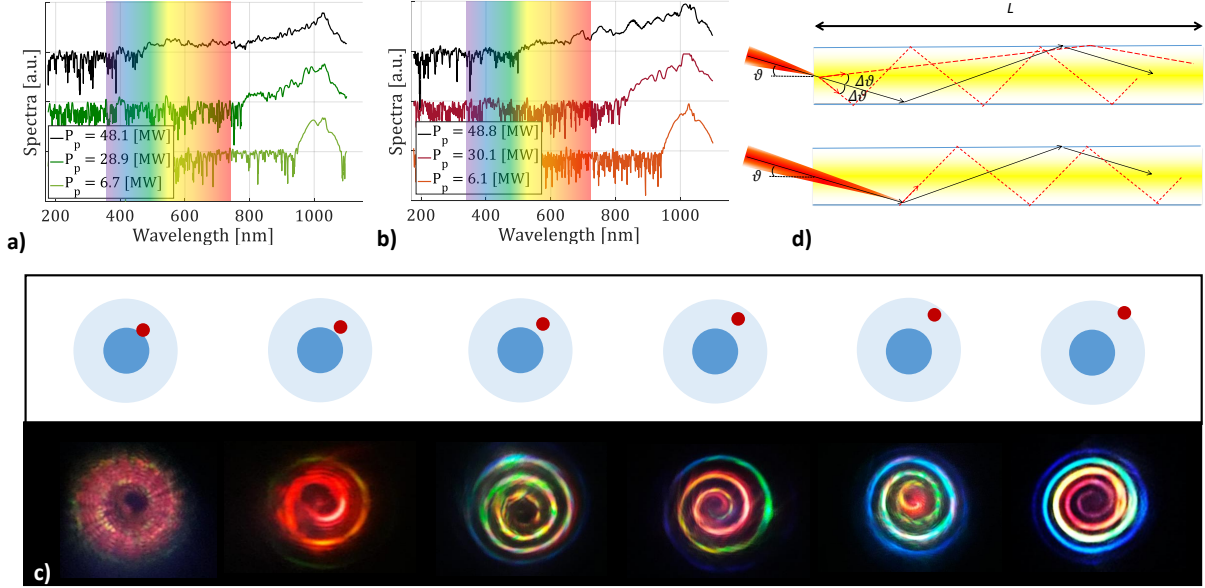


Figure 3: (a-b) fibre output spectra at different input peak powers (up to 48 MW) at 1030 nm in step- and graded-index fibres respectively keeping the same coupling conditions. (c) Far-field image of graded-index fibre when varying the input beam position keeping the peak power at 48 MW, while keeping $\vartheta = 1.5^\circ$ and $\varphi = 45^\circ$. (d) Ray optics sketch of conical emission analogy. On the top, the SC is generated inside the fiber volume. On the bottom, the case of SC generates at the air-cladding interface.

During the experiments, we observed that the shape of the spiral emission strictly depends on the specific input coupling conditions. The configuration where $TC = 1$ is obtained when the input beam wave vector radial component is vanishing. In Fig.4a we report the particular case of a beam focused on the cladding-air interface: here the black arrow indicates the in-plane component of the wave vector. This configuration gives rise to a rainbow spiral emission in both SI and GRIN fibres, as illustrated in Fig.4b and c, respectively. If one reverses the direction of the arrow (i.e., by rotating the azimuthal angle), the topological charge of the spiral flips its sign (see Fig.4d-e). However, one can have intermediate configurations, where the radial component of the wave vector is nonzero. We show in Fig.4f-g an example of input coupling condition, for which the beam appears as a superposition of spirals with $TC = \pm 1$. One can remark the formation of a heart shape at the centre of the far-field image. In the extreme case, where the transverse component of the wave vector is directed along the radius (Fig.4h), the two counter-rotating spirals have exactly the same intensity, producing the far-field which is shown in (Fig.4i). This configuration is bistable, and in the presence of small fluctuations one may observe a decay in complex far-field patterns. Finally, we report in Fig.4j a case where an output beam with $TC = 2$ is produced.

Discussion

The observed spiral emission can be explained by the analogy with the spatial generation of OAM modes from single filaments in air [20, 21]. This manifests when an intense laser pulse increases the air refractive index, owing to the Kerr effect. As a consequence, the pulse collapses, and a plasma channel is generated along the optical axis. When the beam self-focusing and plasma defocusing compensate for each other, the pulse transforms into a filament, surrounded by an energy reservoir. This is analogous to light propagating in optical fibres: the plasma channel acts as the core, and the energy reservoir as the cladding [21]. Upon propagation in the filament, a portion of radiation is lost, being emitted at

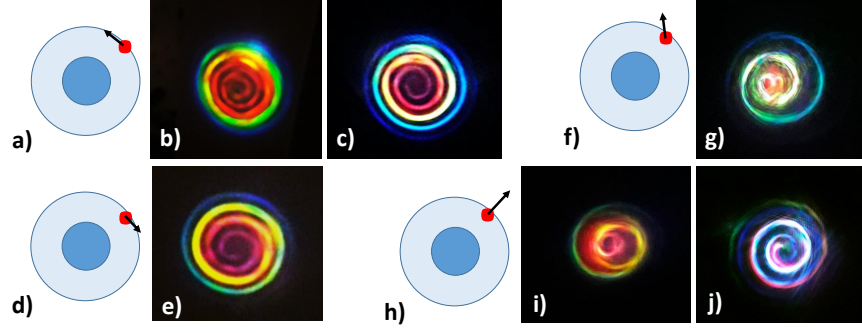


Figure 4: (a) Sketch of the input configuration for rainbow spiral emissions obtained in either SI (b) or GRIN (c) fibres. Black arrows represent the transverse plane component of the input wave vector. (d) Symmetric situation with respect to (a), leading to flipping the topological charge which results in a change of chirality, as seen in (e). (f-g) Superposition of two spirals ($TC = \pm 1$) with different intensities (g) (heart-like spiral emission), when the transverse wave vector has a nonzero radial component (f). (h-i) Same as in (f-g), when the transverse wave vector points along the radial direction. (j) Bistable case, resulting in a spiral beam with $TC = 2$. For all pictures shown, the input power and wavelength were 48 MW and 1030 nm, respectively and the fibres were 2 cm long. All the images but (b) refer to GRIN fibres.

specific angles, a process known as conical emission [26, 27, 28, 29, 30, 31, 32]. Recently, Walter et al. demonstrated OAM beam generation by means of deformable mirrors, transforming conical emission into a spiral [20, 21]. The latter is due to the difference of group velocity between the plasma channel and the energy reservoir, which allows for a continuous interaction between their modes. The background energy flows helically around the plasma channel (just as seen in Fig. 1c), thus slightly deviating the filament, and impressing wavefront rotation. In fibres, nonlinearity is not necessary to obtain OAM beams, because the cladding (reservoir) and the core (filament) are defined by the linear index profile. Moreover, no external spatial modulation is needed, since the cladding geometry spontaneously creates OAM when a symmetry-breaking is seeded by a small tilt of the transverse incidence angle.

The analogy with radiation emission by single filaments in air allows for understanding the mechanism of colour separation in rainbow SC spiral emission. In conical emission, shorter wavelengths are emitted with wider angles in the presence of SC generation. The wavelength spread produced by source broadening depends on the Kerr effect-induced electron density gradient: the larger the gradient, the more shifted the generated wavelengths. When SC is generated, its wave vector has a radial component whose modulus linearly grows with optical frequency. This results in a narrower (larger) angle of emission for long (short) wavelengths. In particular, since the radial electron density gradient varies continuously from zero to a maximum value, rainbow rings are generated. This phenomenon has been attributed to self-phase modulation (SPM) in the radial direction [33, 34, 35].

Applied to our case, the mathematical model to describe the frequency- angular intensity distribution of spectral components $S_{an}(\vartheta, \lambda, z)$ is [35]

$$S_{an}(\vartheta, \lambda, z) = S_0(\vartheta, \lambda, z)\ell(z)^2 \text{sinc} \frac{\Delta\vartheta}{2}, \quad (1)$$

where $\Delta\vartheta$ is the phase excursion of radiation from a broadband point source with distribution S_0 and propagating with group velocity v_g over distance $\ell(z)$ which reads as [35]

$$\Delta\vartheta = \frac{2\pi\ell(z)}{\lambda_0} \left[\left(1 - \frac{\lambda_0}{\lambda}\right) \frac{c_0}{v_g} - \left(1 - \frac{\lambda_0 n(\lambda)}{\lambda n_0} \cos(\vartheta)\right) n_0 \right]. \quad (2)$$

Here n_0 is the refractive index, $n(\lambda)$ is material dispersion in silica, and c_0 the speed of light in vacuum. Since we spontaneously generate an OAM beam, the helical path of the photon now leads to rainbow-like spiral emission, instead of a conical emission. The filamentation analogy also helps to explain the colour separation shown in Fig. 3c. Whenever SC generation takes place inside the cladding volume, the pump propagation direction is locally a symmetry axis, and two wavevectors are associated with the same wavelength, which is equivalent to conical emission. This configuration is sketched on the top of Fig. 3d by an intuitive ray-optics picture. The initial spread $2\Delta\theta$ gets wider after each reflection, leading to interference which is responsible for colour mixing in the far-field. One can estimate that very small emission angles ($\Delta\theta < 10^{-5} \text{ rad}$) are needed in order to incur into interference. Things drastically change when the input beam

is focused right at the cladding-air interface (bottom of Fig.3d). This is because the cladding edge breaks the symmetry along the beam propagation, and a one-to-one correspondence between wavelength and wavevector is imposed by the electromagnetic field continuity condition at the boundary. The resulting lonely ray does not suffer from any interference, and a rainbow colour distribution is observed as in the case of conical emission in air.

Conclusion

We observed the generation of multicolour spiral beam by using standard commercial silica optical fibres. The main trick consists of choosing appropriate fibre coupling conditions, in order to excite cladding modes that carry OAM, and to combine them with the self-focusing process, which permits to generate a large spectral broadening. Our method of OAM beam generation has several advantages. First of all, employing optical fibres allows for easier integration with existing devices and, while in conventional OAM beam generators one has to rely on spatial light modulators, here OAM is intrinsically provided by the cylindrical geometry of the fibre. Moreover, the method is quite robust: it does not depend on the source state polarization, power and wavelength. The spiral emission formation in fibres is analogous to light filamentation in air. Accordingly, in analogy with conical emission, we could explain the observed rainbow spiral emission in MMFs. Our results provide a substantial advance in structured light generation, and pave the way to the practical application of OAM beams in data storage, super-resolution and nanoscale microscopy technologies. Moreover, since OAM beams are a phenomenon that is shared by classical and quantum physics, our generation approach might find applications in quantum optics. Thanks to the low sensitivity to environmental perturbations with respect to in-air OAM beam generation, our method can be applied to implement immersible optical tweezers for applications in biology as well.

3 methods

3.1 Beam spiralling top view

The top view images in Fig.1c-e were taken with a Dinolight2.0 digital microscope for 140 mW average input power from the femtosecond laser at 1030 nm, at the repetition rate of 20 kHz. One can appreciate that part of the beam propagates inside the fibre core in Fig.1d. In fact, the periodicity of the violet emission intensity is due to the spatial self-imaging effect, i.e. the periodic oscillation of the beam intensity induced by parabolic index grading [22]. As a confirmation, these intensity oscillations are absent when a step-index fibre is used (see Fig.1e). Moreover, one can appreciate that the scattered light in the step-index does not have a blue component due to the absence of Germanium doping.

3.2 Experimental Setup

Our pulsed light source was a Yb-based laser (Light Conversion PHAROS-SP-HP), generating pulses of 180 fs with 1-100 kHz repetition rate. The laser beam was focused on the input facet of the fibre, and incident with a controllable tilt angles ϑ and φ with respect to the fibre axis z , and with a beam diameter of about $10 \mu\text{m}$ at $1/e^2$ of peak intensity. Both the parabolic GRIN fibre and the step-index fibre had a core radius $r_c=25 \mu\text{m}$, cladding radius $62.5 \mu\text{m}$, and a cladding index $n_{\text{clad}}=1.45$ at $\lambda = 1030 \text{ nm}$. The relative core-cladding index difference was $\Delta=0.0103$ or 0.0120 for the GRIN and the step-index fibre, respectively. The index grading is realized by Germanium doping. Spectra were collected by a miniature fibre optics spectrometer (Ocean Optics USB2000+), with 200-1100 nm spectral range and an optical spectrum analyzer (OSA) (Yokogawa AQ6370D), while far and near-field images were taken by a Reflex digital camera (Nikon D850) and a Gentec Beamage-4M-IR CCD camera, respectively. Input and output average powers were measured by a thermopile power meter (GENTEC XLP12-3S-VP-INT-D0). Our CW light source was a 4 mW HeNe-based laser (Thorlabs HNLS008L-EC).

3.3 Numerical model

The numerical model developed to describe the process of generation and propagation of OAM beams and spiral emission in MMFs is the $(3D + 1)$ GNLSE (or Gross-Pitaevskii equation [36]) in its vectorial form, involving a single

field for each polarization, including all frequencies and modes [25]:

$$\begin{aligned} \frac{\partial A_p(x, y, z, t)}{\partial z} = & \frac{i}{2k} \left(\frac{\partial^2 A_p}{\partial x^2} + \frac{\partial^2 A_p}{\partial y^2} \right) - i \frac{\beta_2}{2} \frac{\partial^2 A_p}{\partial t^2} + \frac{\beta_3}{6} \frac{\partial^3 A_p}{\partial t^3} + i \frac{\beta_4}{24} \frac{\partial^4 A_p}{\partial t^4} - \frac{\alpha}{2} A_p + \\ & + i \frac{k}{2} \left[\frac{n^2(x, y)}{n_0^2} - 1 \right] A_p + i \gamma \left(1 + i K_2 + \frac{i}{\omega_0} \frac{\partial}{\partial t} \right) \left[(1 - f_R) A_p \left(|A_p|^2 + \frac{2}{3} |A_q|^2 + \frac{1}{3} A_p^2 e^{-2i\omega_0 t} \right) + \right. \\ & \left. + f_R A_p \int_{-\infty}^t d\tau h_R(\tau) \left(|A_p(t - \tau)|^2 + \frac{2}{3} |A_q(t - \tau)|^2 \right) \right] \end{aligned} \quad (3)$$

with $k = n_0 \frac{2\pi}{\lambda}$, $\gamma = n_2 \frac{2\pi}{\lambda}$, $K_2 = \frac{\alpha_2}{2\gamma}$, and $f_R = 0.18$. In Eq.(3), the two polarizations $p, q = x, y$ are nonlinearly coupled. Terms in the right-hand side of Eq. (3) account for: transverse diffraction, second, third and fourth-order dispersion, linear loss, the waveguiding term with refractive index profile $n(x, y)$ and core index n_0 , Kerr and Raman nonlinearities (with nonlinear coefficient γ and fraction f_R), respectively. In Eqs.(3) we neglect the contribution of polarization mode dispersion: we numerically verified that its effects are negligible for the short fibre lengths (few centimeters) involved in our experiments. Nonlinearities include self-steepening, third-harmonic generation (THG) and two-photon absorption (TPA) (with coefficient α_2).

In simulations, we used the following GRIN fibre parameters: core radius, cladding radius, and relative index difference are already provided in the experimental setup subsection; dispersion parameters are $\beta_2 = 18.9 \text{ ps}^2/\text{km}$ at 1030 nm, $\beta_3 = 0.041 \text{ ps}^3/\text{km}$, $\beta_4 = -5.3 \times 10^{-5} \text{ ps}^4/\text{km}$; nonlinear parameters are $n_2 = 2.7 \times 10^{-20} \text{ m}^2/\text{W}$, $\alpha_2 = 1 \times 10^{-16} \text{ m/W}$; $h_R(\tau)$ with the typical response times of 12.2 and 32 fs, respectively [37, 38]. We included the wavelength dependence of the linear loss coefficient α , as reported for standard SM glass fibres [39]. The input beam was modeled as a Gaussian beam with $w_0 = 5 \text{ }\mu\text{m}$ waist (10 μm diameter); we used a Gaussian temporal shape with full-width-at-half-maximum (FWHM) pulse-width $T_{\text{FWHM}} = 180 \text{ fs}$. The input beam was coupled at different points of the cladding or the core, and tilted by small angles (up to 15 degrees).

4 Supplementary materials

4.1 Spiral emission as a function of input pulse duration, peak power, and wavelength.

The objective of this section is to show that spiral emission by injecting a laser beam in the cladding of an optical fibre is not affected by a change of different parameters of the source beam. We demonstrate that, by showing images of the far-field at the fibre output, when we vary either the peak power, the time duration of the incident laser pulse, or the source wavelength. Fig.5a and b show far-field (first two rows) and near-field images (third row) at the output of 2 cm long GRIN or SI fibres. The near-field is only reported for the GRIN fibre case. Here the wavelength and the pulse duration are kept at 1030 nm and 180 fs, respectively, while the input peak power is varied between 0.1 MW and 6 MW. These values remain below the SC generation threshold, so that spiral emission is only observed in the near-IR (i.e., at the pump wavelength). By comparing the different images, we can see that that only intensity variations occur (owing to the increase of input power), while the spiral shape remains unchanged. Fig.5b shows the evolution of the far-field intensity from the output of a 2 cm length of GRIN MMF at 1030 nm, with 0.1 mW of input average power, when the pulse duration is varied from 180 ps to 8 ps. As we can see, spiral generation is independent of the time duration of the input pulse as well, which confirms the linear nature of the phenomenon.

We confirmed that spiral beams can always be obtained, also when the pump wavelength is varied from 1030 nm. In Fig.6a and b we show the far-field at the output of GRIN and SI fibres, respectively, when the input wavelength ranges from 650 nm to 940 nm, while keeping the same incidence angle and position of the input beam. In Fig.6c and d we report the corresponding near-field distributions and spectra for the case of a GRIN fibre only. Again, we can remark that the formation of far-field spiral shapes is always observed, for any value of the source wavelength. In Fig.6e we report the spectra obtained from GRIN MMFs, when varying the input peak power up to 49 MW.

4.2 Spiral emission from singlemode fibre and from laser pointer

The objective of this section is to demonstrate, both experimentally and numerically, spiral emission from an SMF. Fig.7a schematically illustrates the input coupling condition. The laser beam is offset by about 45 μm with respect to the fibre axis, with $\vartheta = 1.5^\circ$ and $\varphi = 45^\circ$. Figures 7b,c show the far-field image at the output of a 2 cm long SMF, as obtained either experimentally or numerically, under the same conditions. The wavelength and the pulse duration were kept at 1030 nm and 180 fs, respectively, while the input peak power was 0.1 MW, and the repetition rate was 50 kHz. As can be seen from these images, even in the case of a singlemode core it is possible to generate spiral emission out of

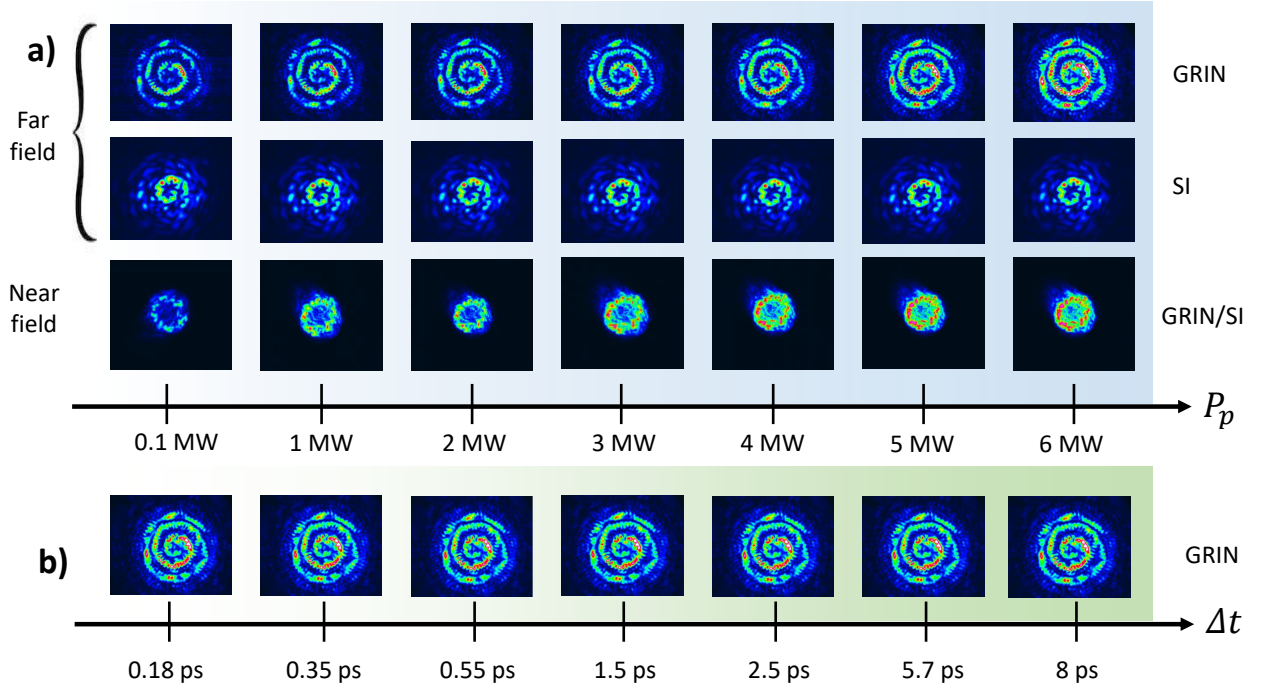


Figure 5: (a) Near and far-field images at the output of a 2 cm GRIN or SI fibre. The input peak power varies from 0.1 MW to 6 MW, with a repetition rate 50 kHz. The source wavelength is 1030 nm, while the fibres are 1.5 cm long. The coupling angles are $\vartheta = 2^\circ$ and $\varphi = 45^\circ$. (b) Far-field images from GRIN fibre, under the same conditions as (a). Here the input average power is maintained at 0.1 mW, while the pulse duration varies between 0.18 to 8 ps

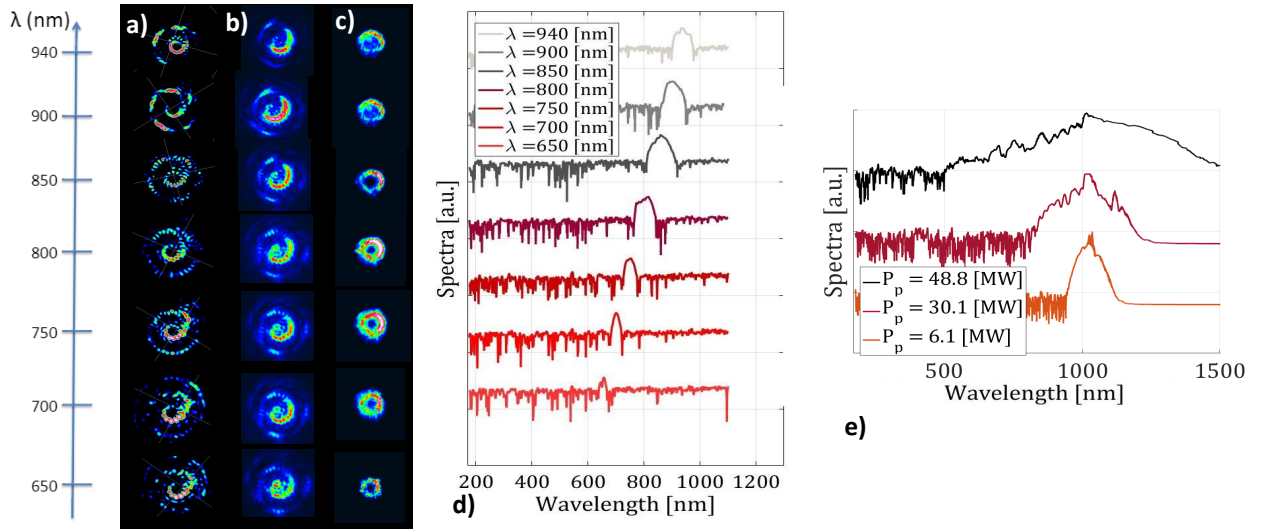


Figure 6: (a) Far-field images from a 2 cm long GRIN when the wavelength of the laser source varies between 650 and 940 nm. The input power is kept at 0.1 MW, with a 50 kHz repetition rate; the input beam coupling angles are $\vartheta = 2^\circ$ and $\varphi = 45^\circ$. (b) Same as in (a), for a SI fibre. (c-d) Near-field output intensity and spectra corresponding to (a). (e) fibre output spectra at different input peak powers (up to 48 MW) at 1030 nm in GRIN fibres keeping the same coupling conditions.

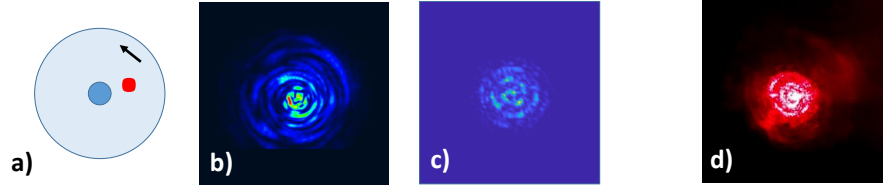


Figure 7: (a) Sketch of the input coupling configuration for spiral emissions in an SMF. Black arrows represent the in-plane component of the input wave vector. (b) Experimental and (c) numerical far-field images from a 2 cm long SMF at 1030 nm. The input peak power is 0.1 MW with a repetition rate of 50 kHz, and the coupling angles are $\vartheta = 2^\circ$ and $\varphi = 45^\circ$. (d) Spiral emission from a commercial laser pointer.

the fibre, by suitably coupling the incoming laser beam with the fibre cladding. Additionally, in Fig.7d we report the far-field image from GRIN MMFs, using a commercial laser pointer.

4.3 OAM impressed by cladding modes

We have shown in the main text, both numerically and experimentally, that the output spiral shape forms in the far field at the fibre output if and only if the input beam is coupled with the cladding. Here, we analytically demonstrate that OAM modes are indeed supported by the fibre cladding. OAM modes can be generated by the combination of two fundamental cylindrical vector (CV) modes, i.e. $OAM_{\pm\ell,m} = TM_{\ell,m} \pm iTE_{\ell,m}$, with $m = 0, 1, \dots, \ell$ [12]. We refer to ℓ as the topological charge TC , so that when $TC = 1$, $OAM_{\pm,m1} = TM_{1,m} \pm iTE_{1,m}$. Let us consider the simplest case of SI fibre, with axially symmetric profile and dielectric permittivity $\varepsilon(r)$. For a cylindrical fibre, the electric and magnetic fields can be written as [24, 40]:

$$\mathbf{E}(r, \varphi, z, t) = \mathbf{E}_0(r)e^{\beta z - \omega t - \ell\varphi} \quad (4)$$

$$\mathbf{H}(r, \varphi, z, t) = \mathbf{H}_0(r)e^{\beta z - \omega t - \ell\varphi} \quad (5)$$

having indicated with β , ω and φ the propagation constant, the angular frequency and the azimuthal number, respectively. Using Maxwell's equations in cylindrical coordinates, we obtain a differential equation, whose solutions can be expressed as a superposition of Bessel's functions of the first and second kind.

$$E_z = i \frac{u^2}{k_0 \varepsilon} (AJ_\ell + BY_\ell) \quad (6)$$

$$E_z = -\frac{u^2}{k_0} (CJ_\ell + DY_\ell) \quad (7)$$

where $k_0 = \omega/c$, $u = \sqrt{k_0^2 \varepsilon - \beta^2}$, J and Y stand for the wave number, the transverse component of the wave vector, and the first and second kind of Bessel function, respectively. The coefficients A , B , C , and D are computed by imposing boundary conditions between separation interfaces, i.e., by imposing the continuity of the tangential components of the fields between the various layers (core/cladding and cladding/air). To this aim, it is useful to express the field in a matrix form in the three layers: in the core, being $\sigma = \beta\ell/k_0$, [24, 40]

$$\begin{pmatrix} E_z & H_z & E_\varphi & H_\varphi \end{pmatrix}^T = [M_{cor}] \begin{pmatrix} A_1 & 0 & C_1 & 0 \end{pmatrix}^T \quad (8)$$

with

$$[M_{cor}] = \begin{pmatrix} i \frac{u_{cor}^2}{\varepsilon_{cor} k_0} J_\ell(u_{cor} r) & 0 & 0 & 0 \\ 0 & 0 & -\frac{u_{cor}^2}{k_0} J_\ell(u_{cor} r) & 0 \\ -i \frac{\sigma}{r \varepsilon_{cor}} J_\ell(u_{cor} r) & 0 & i u_{cor} J'_\ell(u_{cor} r) & 0 \\ -u_{cor} J'_\ell(u_{cor} r) & 0 & \frac{\sigma}{r} J_\ell(u_{cor} r) & 0. \end{pmatrix} \quad (9)$$

Analogously, in the cladding

$$\begin{pmatrix} E_z & H_z & E_\varphi & H_\varphi \end{pmatrix}^T = [M_{cla}] = \begin{pmatrix} A_2 & 0 & C_2 & 0 \end{pmatrix}^T \quad (10)$$

with

$$[M_{cla}] = \begin{pmatrix} i \frac{u_{cla}^2}{\varepsilon_{cla} k_0} J_\ell(u_{cla} r) & i \frac{u_{cla}^2}{\varepsilon_{cla} k_0} Y_\ell(u_{cla} r) & 0 & 0 \\ 0 & 0 & -\frac{u_{cla}^2}{k_0} J_\ell(u_{cla} r) & -\frac{u_{cla}^2}{k_0} Y_\ell(u_{cla} r) \\ -i \frac{\sigma}{r \varepsilon_{cla}} J_\ell(u_{cla} r) & 0 & i u_{cla} J'_\ell(u_{cla} r) & i u_{cla} Y'_\ell(u_{cla} r) \\ -u_{cla} J'_\ell(u_{cla} r) & -u_{cla} Y'_\ell(u_{cla} r) & \frac{\sigma}{r} J_\ell(u_{cla} r) & \frac{\sigma}{r} Y_\ell(u_{cla} r) \end{pmatrix} \quad (11)$$

Unlike the core case, the origin of the reference system does not belong to the cladding (due to its annular shape). This allows to take into account Bessel functions of the second kind, whose contribution in the core had to be suppressed in 9, since it produces a divergence in $r = 0$. Finally, in the last layer made up of air surrounding the fibre, since the field decays to zero at the infinity, one must impose that $A_3 = C_3 = 0$.

$$\begin{pmatrix} E_z & H_z & E_\varphi & H_\varphi \end{pmatrix}^T = [M_{air}] = \begin{pmatrix} A_3 & 0 & C_3 & 0 \end{pmatrix}^T \quad (12)$$

$$[M_{air}] = \begin{pmatrix} 0 & i \frac{u_{air}^2}{\varepsilon_{air} k_0} K_\ell(u_{air} r) & 0 & 0 \\ 0 & 0 & 0 & -\frac{u_{air}^2}{k_0} K_\ell(u_{air} r) \\ 0 & -i \frac{\sigma}{r \varepsilon_{air}} K_\ell(u_{air} r) & 0 & i u_{air} K'_\ell(u_{air} r) \\ 0 & -u_{air} K'_\ell(u_{air} r) & 0 & \frac{\sigma}{r} K_\ell(u_{air} r) \end{pmatrix} \quad (13)$$

where K is the modified Bessel function, and $u_{air} = \sqrt{-k_0^2 \varepsilon_{air} + \beta^2}$.

Imposing now the boundary condition on each separation interface, we have

$$[M_{cor}(r_{cor})] \begin{pmatrix} A_1 & 0 & C_1 & 0 \end{pmatrix}^T = [M_{cla}(r_{cor})][M_{cla}^{-1}(r_{cla})][M_{air}(r_{cla})] \begin{pmatrix} 0 & B_3 & 0 & D_3 \end{pmatrix}^T \quad (14)$$

By solving the matrix system it is possible to obtain the problem unknowns. In our case, being $\frac{n_{cor} - n_{cla}}{n_{cla}} \ll 1$ and using the zero-order paraxial approximation, we find that for TE_{0m} modes

$$E_r = 0 \quad E_\varphi = i E_{1m}(r) \quad (15)$$

$$H_r = -\frac{\beta_{1m}}{\omega \mu_0} E_{1m}(r) \quad H_\varphi = 0 \quad (16)$$

and for TM_{0m} modes

$$E_r = E_{1m}(r) \quad E_\varphi = 0 \quad (17)$$

$$H_r = 0 \quad H_\varphi = \frac{\beta_{1m}}{\omega \mu_0} E_{1m}(r) \quad (18)$$

with $E_{1m} = A J_1 + B Y_1$. The $TM_{0,m}$ and $TE_{0,m}$ modes, necessary for the generation of the OAM modes $OAM_{\pm 1,m} = TM_{0,m} + i TE_{0,m}$, are therefore supported by the cladding of optical fibres. In order to obtain a circular combination of the two modes, it is sufficient to enter with an appropriate angle into the cladding, as we have discussed in the main text.

Acknowledgements

This work has received funding from the European Union Horizon 2020 research and innovation program under the European Research Council Advanced Grant No. 740355 (STEMS), the Marie Skłodowska-Curie Grant No. 713694 (MULTIPLY), and the Russian Ministry of Science and Education Grant No. 14.Y26.31.0017. A.T., V.C., and T. M. acknowledge the financial support provided by: the French ANR through the ‘‘TRAFIC project: ANR-18-CE080016-01’’; the CILAS Company (ArianeGroup) through the shared X-LAS laboratory; the ‘‘Région Nouvelle Aquitaine’’ through the projects F2MH and Nematum; the National Research Agency under the Investments for the future program with the reference ANR-10-LABX-0074-01 Sigma-LIM.

Author contributions

FM and M.F. carried out the experiments, M.Z. developed and performed the numerical simulations. All authors analysed the obtained results, and participated in the discussions and in the writing of the manuscript.

The authors declare that they have no competing financial interests.

Correspondence and requests for materials should be addressed to Fabio Mangini (email: fabio.mangini@unibs.it).

References

- [1] Logan G Wright, Demetrios N Christodoulides, and Frank W Wise. Controllable spatiotemporal nonlinear effects in multimode fibres. *Nature Photonics*, 9(5):306–310, 2015.
- [2] Hu Zhang, Xiaoguang Zhang, Hui Li, Yifan Deng, Lixia Xi, Xianfeng Tang, and Wenbo Zhang. The orbital angular momentum modes supporting fibers based on the photonic crystal fiber structure. *Crystals*, 7(10):286, 2017.
- [3] Hongwei Zhang, Baiwei Mao, Ya Han, Zhi Wang, Yang Yue, and Yange Liu. Generation of orbital angular momentum modes using fiber systems. *Applied Sciences*, 9(5):1033, 2019.
- [4] Les Allen, Marco W Beijersbergen, RJC Spreeuw, and JP Woerdman. Orbital angular momentum of light and the transformation of Laguerre-Gaussian laser modes. *Physical Review A*, 45(11):8185, 1992.
- [5] Jian Wang, Jeng-Yuan Yang, Irfan M Fazal, Nisar Ahmed, Yan Yan, Hao Huang, Yongxiong Ren, Yang Yue, Samuel Dolinar, Moshe Tur, et al. Terabit free-space data transmission employing orbital angular momentum multiplexing. *Nature Photonics*, 6(7):488–496, 2012.
- [6] Nenad Bozinovic, Yang Yue, Yongxiong Ren, Moshe Tur, Poul Kristensen, Hao Huang, Alan E Willner, and Siddharth Ramachandran. Terabit-scale orbital angular momentum mode division multiplexing in fibers. *Science*, 340(6140):1545–1548, 2013.
- [7] Robert Fickler, Geoff Campbell, Ben Buchler, Ping Koy Lam, and Anton Zeilinger. Quantum entanglement of angular momentum states with quantum numbers up to 10,010. *Proceedings of the National Academy of Sciences*, 113(48):13642–13647, 2016.
- [8] NR Heckenberg, R McDuff, CP Smith, and AG White. Generation of optical phase singularities by computer-generated holograms. *Optics Letters*, 17(3):221–223, 1992.
- [9] Homayoon Oraizi and Hedieh Emamian. Generation of orbital angular momentum modes via holographic leaky-wave metasurfaces. *Scientific Reports*, 10(1):1–13, 2020.
- [10] NB Simpson, L Allen, and MJ Padgett. Optical tweezers and optical spanners with Laguerre–Gaussian modes. *Journal of Modern Optics*, 43(12):2485–2491, 1996.
- [11] Xiaowei Zhuang. Unraveling DNA condensation with optical tweezers. *Science*, 305(5681):188–190, 2004.
- [12] Yijie Shen, Xuejiao Wang, Zhenwei Xie, Changjun Min, Xing Fu, Qiang Liu, Mali Gong, and Xiaocong Yuan. Optical vortices 30 years on: OAM manipulation from topological charge to multiple singularities. *Light: Science & Applications*, 8(1):1–29, 2019.
- [13] Andrew Forbes, Angela Dudley, and Melanie McLaren. Creation and detection of optical modes with spatial light modulators. *Advances in Optics and Photonics*, 8(2):200–227, 2016.
- [14] Yan Zhang, Zhiyong Bai, Cailing Fu, Shen Liu, Jian Tang, Jian Yu, Changrui Liao, Ying Wang, Jun He, and Yiping Wang. Polarization-independent orbital angular momentum generator based on a chiral fiber grating. *Optics Letters*, 44(1):61–64, 2019.
- [15] Ya Han, Yan-Ge Liu, Zhi Wang, Wei Huang, Lei Chen, Hong-Wei Zhang, and Kang Yang. Controllable all-fiber generation/conversion of circularly polarized orbital angular momentum beams using long period fiber gratings. *Nanophotonics*, 7(1):287–293, 2018.
- [16] Youchao Jiang, Guobin Ren, Ya Shen, Yao Xu, Wenxing Jin, Yue Wu, Wei Jian, and Shuisheng Jian. Two-dimensional tunable orbital angular momentum generation using a vortex fiber. *Optics Letters*, 42(23):5014–5017, 2017.
- [17] G Prabhakar, P Gregg, L Rishoj, P Kristensen, and S Ramachandran. Octave-wide supercontinuum generation of light-carrying orbital angular momentum. *Optics Express*, 27(8):11547–11556, 2019.
- [18] Wei Huang, Yan-ge Liu, Zhi Wang, Wanchen Zhang, Mingming Luo, Xiaoqi Liu, Junqi Guo, Bo Liu, and Lie Lin. Generation and excitation of different orbital angular momentum states in a tunable microstructure optical fiber. *Optics Express*, 23(26):33741–33752, 2015.
- [19] Zeinab Sanjabi Eznavah, Juan Carlos Alvarado Zacarias, Jose Enrique Antonio Lopez, Kai Shi, Giovanni Milione, Yongmin Jung, Benn C Thomsen, David J Richardson, Nicolas Fontaine, Sergio G Leon-Saval, et al. Photonic lantern broadband orbital angular momentum mode multiplexer. *Optics Express*, 26(23):30042–30051, 2018.
- [20] Dominik Walter, Helge Bürsing, and Reinhard Ebert. Emission of spiral patterns from filaments in the infrared. *Optics Express*, 18(23):24258–24263, 2010.

- [21] Dominik Walter, Helge Bürsing, and Reinhard Ebert. Emissions from single filaments in air triggered by tailored background energy flows. *Optics Letters*, 42(5):931–934, 2017.
- [22] Tobias Hansson, Alessandro Tonello, Tigran Mansuryan, Fabio Mangini, Mario Zitelli, Mario Ferraro, Alioune Niang, Rocco Crescenzi, Stefan Wabnitz, and Vincent Couderc. Nonlinear beam self-imaging and self-focusing dynamics in a GRIN multimode optical fiber: theory and experiments. *Opt. Express*, 28(16):24005–24021, Aug 2020.
- [23] Fabio, Mario Mangini, Mario Ferraro, Alioune Zitelli, Alessandro Niang, Vincent Tonello, Stefan Couderc, and Wabnitz. Multiphoton absorption excited upconversion luminescence in optical fiber. *ArXiv*, Sep 2020.
- [24] Oleg V Ivanov, Sergei A Nikitov, and Yurii V Gulyaev. Cladding modes of optical fibers: properties and applications. *Physics-Uspokhi*, 49(2):167, 2006.
- [25] Mario Zitelli, Fabio Mangini, Mario Ferraro, Alioune Niang, Denis Kharenko, and Stefan Wabnitz. High-energy soliton fission dynamics in multimode GRIN fiber. *Opt. Express*, 28(14):20473–20488, Jul 2020.
- [26] I Golub. Optical characteristics of supercontinuum generation. *Optics Letters*, 15(6):305–307, 1990.
- [27] ETJ Nibbering, PF Curley, Georges Grillon, BS Prade, MA Franco, François Salin, and André Mysyrowicz. Conical emission from self-guided femtosecond pulses in air. *Optics Letters*, 21(1):62–64, 1996.
- [28] OG Kosareva, VP Kandidov, A Brodeur, CY Chien, and SL Chin. Conical emission from laser–plasma interactions in the filamentation of powerful ultrashort laser pulses in air. *Optics Letters*, 22(17):1332–1334, 1997.
- [29] P Di Trapani, G Valiulis, A Piskarskas, O Jedrkiewicz, J Trull, C Conti, and Stefano Trillo. Spontaneously generated X-shaped light bullets. *Physical Review Letters*, 91(9):093904, 2003.
- [30] C Conti, Stefano Trillo, P Di Trapani, G Valiulis, A Piskarskas, O Jedrkiewicz, and J Trull. Nonlinear electromagnetic X waves. *Physical Review Letters*, 90(17):170406, 2003.
- [31] D Faccio, A Averchi, A Couairon, Miroslav Kolesik, Jerome V Moloney, A Dubietis, G Tamosauskas, P Polesana, A Piskarskas, and P Di Trapani. Spatio-temporal reshaping and X wave dynamics in optical filaments. *Optics Express*, 15(20):13077–13095, 2007.
- [32] Damir Aumiler, Ticijana Ban, and Goran Pichler. Femtosecond laser-induced cone emission in dense cesium vapor. *Physical Review A*, 71(6):063803, 2005.
- [33] Arnaud Couairon and André Mysyrowicz. Femtosecond filamentation in transparent media. *Physics Reports*, 441(2-4):47–189, 2007.
- [34] EO Smetanina, AE Dormidonov, and VO Kompanets. Supercontinuum conical emission accompanying filamentation of a femtosecond laser pulse in fused quartz. *Journal of Optical Technology*, 77(7):463–464, 2010.
- [35] VP Kandidov, EO Smetanina, AE Dormidonov, VO Kompanets, and SV Chekalin. Formation of conical emission of supercontinuum during filamentation of femtosecond laser radiation in fused silica. *Journal of Experimental and Theoretical Physics*, 113(3):422, 2011.
- [36] S. Stringari L. Pitaevskii. *Bose-Einstein Condensation*. Oxford University, 2003.
- [37] R. H. Stolen, J. P. Gordon, W. J. Tomlinson, and H. A. Haus. Raman response function of silica-core fibers. *J. Opt. Soc. Am. B*, 6(6):1159–1166, Jun 1989.
- [38] G. P. Agrawal. *Nonlinear Fiber Optics*. Third edition, Par. 2.3, Academic Pre, 2001.
- [39] E. F. Shubert. *Light-Emitting Diodes*. Cambridge University, 2006.
- [40] M Kong and B Shi. Field solution and characteristics of cladding modes of optical fibers. *Fiber and integrated optics*, 25(4):305–321, 2006.